Ce$_{0.9}$Gd$_{0.1}$O$_{2-x}$ for Intermediate Temperature Solid Oxide Fuel Cells: Influence of Cathode Thickness and Anode Functional Layer on Performance

Visweshwar Sivasankaran [1,2], Lionel Combemale [1] ⓘ**, Mélanie François [1] and Gilles Caboche [1,***ⓘ

[1] Laboratoire Interdisciplinaire Carnot de Bourgogne, ICB-UMR6303, FCLAB, CNRS—Université de Bourgogne, Franche-Comté, 9 Avenue Savary, CEDEX BP47870, 21078 Dijon, France; vsivasankaran@rgipt.ac.in (V.S.); lionel.combemale@u-bourgogne.fr (L.C.); melaniea.francois@gmail.com (M.F.)

[2] Energy Institute Bangalore, A Centre of Rajiv Gandhi Institute of etroleum Technology—Bangalore Center, Nirman Bhavan, Third Floor Dr Rajkumar Road, Rajajinagar I Block, Bengaluru 560 010, India

*** Correspondence: gilles.caboche@u-bourgogne.fr; Tel.: +33-380-39-6153

Abstract: The performances of Intermediate Temperature Solid Oxide Fuel Cell (IT-SOFC) anode-supported planar cells with a 10 cm^2 active surface were studied versus the combination of cathode thickness and the presence of an Anode Functional Layer (AFL). The temperature range was 500 to 650 °C, and Gd$_{0.1}$Ce$_{0.9}$O$_{2-x}$ (GDC) was used as the electrolyte material, Ni-GDC as the anode material, and La$_{0.6}$Sr$_{0.4}$Co$_{0.2}$Fe$_{0.8}$O$_{3-d}$ (LSCF48) as the cathode material. The power density, conductivity, and activation energy of different samples were determined in order to investigate the influence of the cathode thickness and AFL on the performance. These results showed an improvement in the performances when the AFL was not present. The maximum power density reached 370 mW·cm^{-2} at 650 °C for a sample with a cathode thickness of 50 μm and an electrolyte layer that was 20 μm thick. Moreover, it was highlighted that a thinner cathode layer reduced the power density of the cell.

Keywords: tape casting process; open circuit voltage; activation energy; power density; IT-SOFC

1. Introduction

In recent years, there has been more need to develop Intermediate Temperature Solid Oxide Fuel Cells (IT-SOFCs), which work in the range 500–600 °C, compared to the commonly used SOFCs which work in the range 700–1000 °C [1]. A decrease in the SOFC operating temperature can lower the thermal stress on the SOFC stack and widen the types of materials used for structural components in the SOFC systems, which are supposed to provide a reduction in the operation costs and extension of the stack lifetime [2]. However, a reduction in operating temperature may be accompanied by a decrease in the electrochemical performance of each fuel cell system material [3].

Therefore, the choice of the cell materials is restricted to those electrochemically active at the chosen temperature range. Gadolinium-doped ceria (Gd$_{0.1}$Ce$_{0.9}$O$_{2-x}$: GDC) is a promising candidate for SOFC electrolyte at intermediate temperatures thanks to its high ionic conductivity [4], low activation energy, and chemical stability between the room temperature and its melting point.

For the cathode material, lanthanum strontium cobalt iron oxide with the specific composition La$_{0.6}$Sr$_{0.4}$Co$_{0.2}$Fe$_{0.8}$O$_{3±δ}$ (LSCF48) is largely used because of its good chemical compatibility with GDC, its high electro-catalytic properties in the temperature range of 500 to 600 °C, and its thermal expansion coefficient in accordance with the GDC electrolyte [5]. For the anode material, a classical cermet (CERamic plus MEtal) Ni-GDC, showing an excellent electrochemical performance in the case

of the use of pure H_2 as fuel [6], was used. Even though many studies deal with anode thickness and its porosity [7], few of them are interested in the thickness of the cathode and the impact of the Anode Functional Layer (AFL) presence.

This study presents the evolution of the electrical performance with respect to cathode morphology and the presence of an AFL. In order to explain in detail, the maximum power density, activation energies, and Area-Specific Resistance (ASR) measurements obtained at different temperatures were compared on the cells prepared by a single-step sintering process with multilayers.

2. Materials and Methods

2.1. Starting Materials

Commercial-grade $Gd_{0.1}Ce_{0.9}O_{2-x}$ (GDC-10 TC) powder provided by Neyco with a specific surface area of 12.1 $m^2 \cdot g^{-1}$ was chosen as the electrolyte material. NiO commercial nickel oxide from Sigma-Aldrich (99.99% purity with a specific surface area of 3 $m^2 \cdot g^{-1}$) was mixed with GDC powder thoroughly in a weight ratio of 65:35 by ball milling in ethanol for 4 h before bein dried for 13 h at 80 °C to obtain NiO-GDC anode material. For the cathode material, $La_{0.6}Sr_{0.4}Co_{0.2}Fe_{0.8}O_{3\pm\delta}$ (LSCF48) powder was prepared by solid state synthesis at Laboratoire Interdisciplinaire Carnot de Bourgogne (ICB Lab Dijon France).

The initial precursors brought from Sigma Aldrich—strontium carbonate ($SrCO_3$, 99.9%) and oxides of lanthanum (La_2O_3, 99.9%), cobalt (Co_2O_3, 99.0%), and iron (Fe_2O_3, 99.0%) powders—were mixed in a stoichiometric ratio and ball milled for 15 h in ethanol with zirconia balls before being dried for 24 h at 60 °C. Then, the dried powders were calcined at 1100 °C for 24 h with a heating and cooling ramp of 100 °C·h^{-1}. The pure perovskite phase of LSCF48 was confirmed by X-ray diffraction (XRD, D5000, BRUKER Corporation) using Cu Kα_1 radiation (λ = 0.15406 nm), showing no impurities. The specific surface area was determined by the Brunauer–Emmett–Teller (BET) technique to be 0.64 $m^2 \cdot g^{-1}$.

2.2. Slurry Formation for Tape Casting Process

Starting powders have been used as active materials in slurry preparation. Compounds taken at the required weight percentage were mixed in a plastic container. For the preparation of the cathode slurry, LSCF48 was mixed with GDC to make a composite slurry to improve the cell performance by reducing the cathode polarization [8–10]. In this work, a mass ratio of 65:35 for LSCF48 to GDC was chosen, and carbon graphite (5% weight) was added as a pore former.

Concerning the anode material, two slurries were prepared, one with a pore former (5% graphite) for classical porous anode fabrication and the second one without pore former to understand the function of the AFL, between the electrolyte layer and the classical anode layer. The AFL was introduced to the cell to maximize the triple phase boundary (TPB) length and to restrain the activation polarization of the anode [11]. The electrolyte slurry was prepared using GDC powder and was mixed in a Turbula-T2F device with balls of zirconia with a diameter 10 mm for 24 h. This slurry was prepared in two steps, where in the first step GDC was mixed with ethanol and methyl ethyl ketone (MEK) as solvents and triethanolamine (TEA) as a dispersant. In the second step, the binder polyvinyl butyral (PVB) and the plasticizers polyethylene glycol (PEG) and benzylbutyl phthalate (BBP) were added and ball milled for 24 h.

2.3. Tape Casting and Sintering Process

The elaboration of the Membrane-Electrode Assemblies (MEA) composed of dense oxygen-ion-conducting electrolyte (GDC) sandwiched between cathode porous (LSCF-GDC) and anode porous (NiO-GDC) was performed from a multi-layer green tape of the different slurries [12,13]. The cathode slurry was first tape casted on a glass plate using an automatic tape caster (Elcometer) with a casting rate of 1 cm·s^{-1}. The blade gap thickness was fixed, taking into account the sintering shrinkage.

Then, the cathode layer was dried in air at room temperature for 1 h and cut at the desired dimensions before the electrolyte layer was directly tape casted on the cathode layer. After 2 h of drying, the anode functional layer was casted above the electrolyte layer. In the last step, the anode layer was casted on AFL and dried, followed by sintering to obtain an anode-supported IT-SOFC. Figure 1 shows the diagrammatic representation of the process for the elaboration of the four anode-supported planar cells with a 10 cm^2 active surface. Long-term tests were carried out on these single cells manufactured using this process, and they showed a light performance degradation (~9%) after the first 100 h [13].
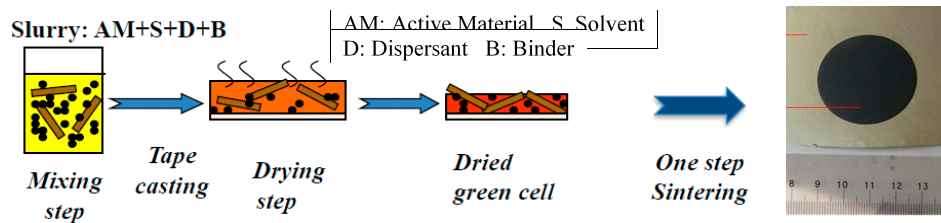

Figure 1. Diagrammatic representation of the elaboration process of the Membrane-Electrode Assemblies (MEAs).

The first MEAs were sintered at 1100, 1215, 1300, and 1400 °C for 5 h with one-hour isothermal at 280 °C, and a heating and cooling rate of 120 K·h^{-1} to determine the best sintering temperature. At 1100 °C, some pores are always present in the electrolyte layer, as shown in Figure 2. When the sintering temperature is higher than 1215 °C the electrolyte layer showed a better density. According to V. Sivasankaran et al. [13,14] and K. Raju et al. [15], the optimized sintering temperature was chosen to be 1215 °C.
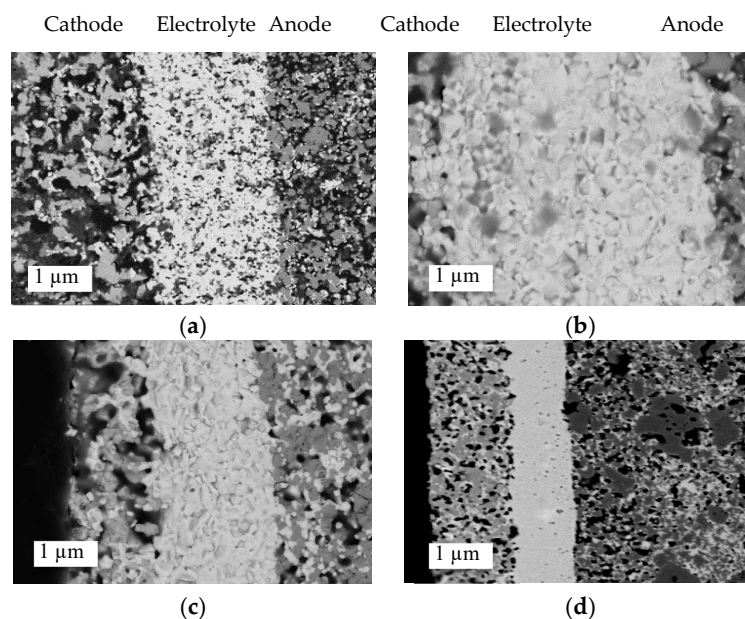

Figure 2. Cross-section of the different MEAs versus the sintering temperature obtained by SEM; the electrolyte layer in the middle shows a high density when the sintering temperature is equal to and over 1215 °C. (**a**) Sintered at 1100 °C; (**b**) sintered at 1215 °C; (**c**) sintered at 1300 °C; (**d**) sintered at 1400 °C.

The cross-sections of the MEAs samples 1 to 4 were observed by Scanning Electron Microscopy (SEM-HITACHI S4200) to determine the thicknesses of the different layers; see Figure 3a,b. In all cases, the electrolyte is very dense and the electrodes are porous. Table 1 gives the features of the different samples in this study. For samples 1 to 3, an AFL layer was deposited between the electrolyte layer

and the classical porous anode-supported layer. For sample 4, the thicknesses of the different layers were optimized and no AFL was present.
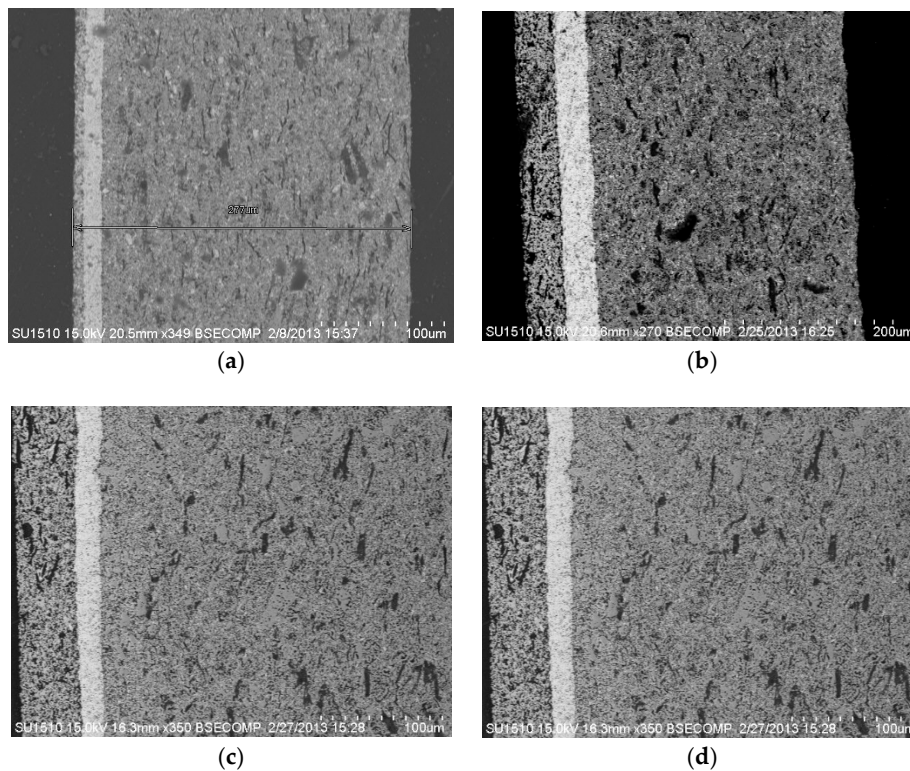

Figure 3. Evolution of the thicknesses of the cathode and electrolyte layers (values are reported in Table 1). (**a**) Cross section of sample 1; (**b**) cross section of sample 2; (**c**) cross section of sample 3; (**d**) cross section of sample 4.

Table 1. Features of the samples studied to improve the density power.

	Cathode Active Area (cm^2)	Thicknesses (µm)			
		Cathode	Electrolyte	Anode Functional Layer	Anode
Sample 1	10	9	15	18	242
Sample 2	10	43	37	33	245
Sample 3	10	48	21	29	249
Sample 4	10	50	20	-	270

3. Results and Discussion

Electrical measurements were conducted using a Fiaxell open flanges device. The cell consisted of a Ni-GDC anode substrate, a functional layer, a GDC electrolyte layer, and a LSCF-GDC cathode. The tests were carried out using a single cell with dimensions of 7.5 cm × 7.5 cm, with an active area of 10 cm^2 and a 3.6 cm diameter of the cathode part (Figure 1). All the samples were tested with gold mesh and nickel felt as current collectors at the cathode and anode sides, respectively. For better gas distribution, an alumina felt was also used at the anode and cathode sides. The samples were then heated at a heating rate of 150 K·h^{-1} in H$_2$(1%)/N$_2$ to 750 °C and retained for 10 min, then the reduction process was continued in pure hydrogen with a flow rate of 500 NmL·min^{-1} at the anode side and air as the cathode gas with a flow rate of 600 NmL·min^{-1}.

After reduction for 2 h, air and a mixture of H$_2$/(3%) H$_2$O were introduced into the cathode and the anode with a flow rate of 1600 and 800 NmL·min^{-1}, respectively. Figure 4a shows *I-V* curves for sample 1 at different temperatures. An Open Circuit Voltage (OCV) of 920 mV at 500 °C was obtained, and it gradually decreases when the temperatures increase. The cell voltage decreases sharply at

500 °C when *I* increases due to a high value of internal resistance, as shown in Table 2. According to J. Li et al. [16], the internal resistance of a SOFC decreases when the temperature increases, leading to an increase in the power values.
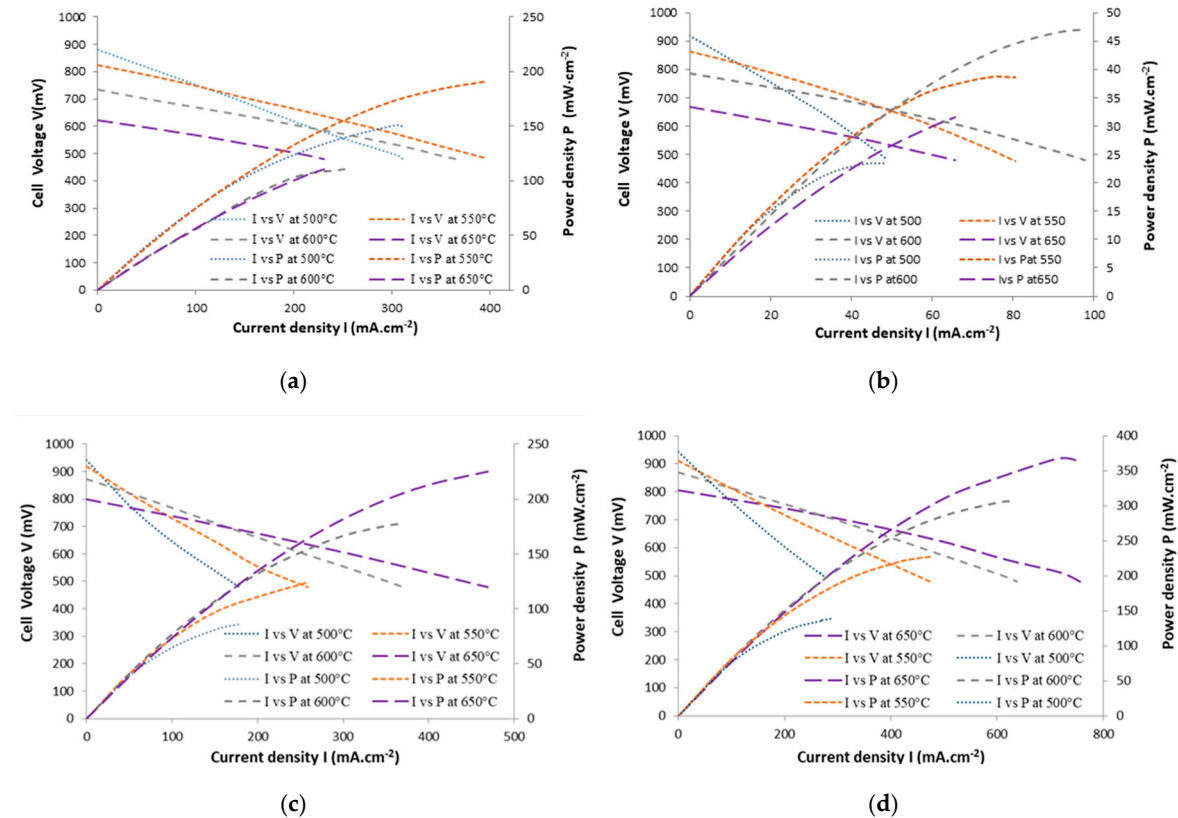

Figure 4. (**a**) *I-V* curves for sample 1 under operation temperatures of: 500, 550, 600, and 650 °C; (**b**) *I-V* curves for sample 2 under operation temperatures of: 500, 550, 600, and 650 °C; (**c**) *I-V* curves for sample 3 under operation temperatures of: 500, 550, 600, and 650 °C; (**d**) *I-V* curves for sample 4 under operation temperatures of: 500, 550, 600, and 650 °C.

The power density reaches 47 mW·cm^{-2}, the maximum value, at 600 °C. Figure 4b shows the *I-V* curves for sample 2 at different temperatures. The OCV is 880 mV at 500 °C and gradually decreases with the increase in the temperature; the power density reaches 190 mW·cm^{-2}, the maximum value, at 550 °C. Figure 4c shows the *I-V* curves for sample 3 at different temperatures. The OCV is 940 mV at 500 °C, and it strongly decreases at 500 °C when *I* increases. At 650 °C, the voltage is more stables versus *I*, and the power density reaches 225 mW·cm^{-2}, the maximum value. Sample 4 gives the best results; in Figure 4d, the OCV is 940 mV at 500 °C. At 650 °C, the voltage is more stable versus *I*, and the power density reaches 370 mW·cm^{-2}.

The OCV theoretical values are calculated using the thermodynamic laws applied to the H$_2$ oxidation and experimental conditions (Equations (1) and (2)). They are equal to 1.15 V at 500 °C and 1.13 V at 650 °C, in accordance with [3,17].

$$E^{OCV} = E^\circ - \frac{RT}{2F} \ln\left(\frac{P_{H_2O}}{P_{H_2}\,P_{O_2}^{0.5}}\right), \tag{1}$$

$$E^\circ = 1.253 - 2.4516 \times 10^{-4}\,T\ (\text{K}). \tag{2}$$

Table 2. The conductivity of the individual layers for the $Gd_{0.1}Ce_{0.9}O_{2-x}$ (GDC)-based Solid Oxide Fuel Cell (SOFC).

Operating Temperature (°C)	σ_{el}, Ionic Conductivity of the Electrolyte (S·cm^{-1}) [18]	σ_{cat}, Electrical Conductivity of the Cathode (S·cm^{-1}) [19]	σ_{an}, Electrical Conductivity of the Anode (S·cm^{-1}) [3]
500	1.32×10^{-3}	1.25	115
550	2.18×10^{-3}	1.37	119
600	3.39×10^{-3}	1.56	122
650	5.04×10^{-3}	1.75	124

The experimental OCVs versus temperatures are reported in Table 3. As usual, the temperature has a negative impact on the OCV value due to the Nernst law. For samples 1 and 2, the OCV values are lower and decrease more sharply than for the samples 3 and 4. The OCV values of samples 1 and 2 are lower than expected due to probable leakages in the open flange setup.

Table 3. Resistance of the individual layers, internal resistance, and ohmic overpotential at different operating temperatures for a specified current density of 200 mA·cm^{-2}.

	Operating Temperature (°C)	$\frac{d_{el}}{\sigma_{el}}$ Resistance of the Electrolyte (Ω)	$\frac{d_{cat}}{\sigma_{cat}}$ Resistance of the Cathode (Ω)	$\frac{d_{an}}{\sigma_{an}}$ Resistance of the Anode (Ω)	R_{ohm} Internal Resistance (Ω)	η_{ohm} Ohmic Overpotential (V)
Sample 1	500	1.14	7.20×10^{-4}	2.35×10^{-4}	1.14	0.228
	550	6.88×10^{-1}	6.57×10^{-4}	2.27×10^{-4}	6.89×10^{-1}	0.138
	600	4.42×10^{-1}	5.77×10^{-4}	2.22×10^{-4}	4.43×10^{-1}	0.089
	650	2.98×10^{-1}	5.14×10^{-4}	2.18×10^{-4}	2.98×10^{-1}	0.060
Sample 2	500	2.80	3.44×10^{-3}	2.42×10^{-4}	2.81	n.d.
	550	1.70	3.14×10^{-3}	2.34×10^{-4}	1.70	n.d.
	600	1.09	2.76×10^{-3}	2.28×10^{-4}	1.09	n.d.
	650	7.34×10^{-1}	2.46×10^{-3}	2.24×10^{-4}	7.37×10^{-1}	n.d.
Sample 3	500	1.59	3.84×10^{-3}	2.42×10^{-4}	1.59	n.d.
	550	9.63×10^{-1}	3.50×10^{-3}	2.34×10^{-4}	9.67×10^{-1}	0.193
	600	6.19×10^{-1}	3.08×10^{-3}	2.28×10^{-4}	6.23×10^{-1}	0.125
	650	4.17×10^{-1}	2.74×10^{-3}	2.24×10^{-4}	4.20×10^{-1}	0.084
Sample 4	500	1.52	4.00×10^{-3}	2.35×10^{-4}	1.52	0.304
	550	9.17×10^{-1}	3.65×10^{-3}	2.27×10^{-4}	9.21×10^{-1}	0.184
	600	5.90×10^{-1}	3.21×10^{-3}	2.22×10^{-4}	5.93×10^{-1}	0.119
	650	3.97×10^{-1}	2.86×10^{-3}	2.18×10^{-4}	4.00×10^{-1}	0.080

By using the cell voltage versus the current density (Figure 4), different behavior, depending on the overpotential contributions, could be evidenced thanks to Equation (3).

$$V = E^{OCV} - \eta_{ohm} - \eta_{act,an} - \eta_{act,cat} - \eta_{conc,an} - \eta_{conc,cat}, \tag{3}$$

where η_{ohm} is the ohmic overpotential, $\eta_{act,an}$ is the activation overpotential due to the anode, $\eta_{act,cat}$ is the activation overpotential due to the cathode, $\eta_{conc,an}$ is the concentration overpotential due to the anode, and $\eta_{conc,cat}$ is the overpotential due to the cathode.

The internal resistance R_{ohm} is defined in Equation (4), and the ohmic overpotential is calculated by Equation (5).

$$R_{ohm} = \frac{d_{el}}{\sigma_{el}} + \frac{d_{cat}}{\sigma_{cat}} + \frac{d_{an}}{\sigma_{an}}, \tag{4}$$

$$\eta_{ohm} = I \times R_{ohm}, \tag{5}$$

where $\frac{d_{el}}{\sigma_{el}}$ corresponds to the resistance of the electrolyte, with d_{el} as the thickness and δ_{el} as the ionic conductivity; $\frac{d_{cat}}{\sigma_{cat}}$ corresponds to the resistance of the cathode, with d_{cat} as the thickness and δ_{cat} as the electrical conductivity; and $\frac{d_{an}}{\sigma_{an}}$ corresponds to the resistance of the anode, with d_{an} as the thickness and δ_{an} as the electrical conductivity.

The conductivity versus temperature of each layer were extracted from the references [3,18,19] and are reported in Table 2. The values of the electrolyte ionic conductivity were carefully selected to correspond to the electrolyte microstructure—i.e., the porosity and grain size of the cells sintered

at 1215 °C. In Table 3, the calculated values of the resistance of each layer and internal resistance lead to the ohmic overpotential versus temperature of each sample for a specified current density of 200 mA·cm^{-2}.

The ohmic overpotential calculated in Table 3 is the major factor of the potential decrease reported in Equation (3). As expected, the influence of the electrolyte on the ohmic potential is largely dominant. The activation overpotentials are not strong enough to cause a decrease in potential for all *I-V* curves, although for samples 3 and 4 at 500 and 550 °C they are slightly noticeable. The concentration overpotential does not account for a significant portion of the potential; Bianchi and al. reported a proportion of ~3% [20]. These results explain the low performance of sample 2 regarding the thickness of the electrolyte layer and its importance in the potential decrease.

In a second step, the Area-Specific Resistance (ASR), which is an important performance parameter, was calculated using the following equation [21,22]:

$$ASR = \frac{OCV - 0.7}{I_{0.7}},$$

where $I_{0.7}$ is the discharging current density at a voltage of 0.7 V.

The results are summarized in Table 4. For samples 1 and 2, the ASR was not calculated at 650 °C because of the low value of OCV, which was inferior to 0.7 V. It is also apparent that the cell 3 and 4 show the lowest values of ASR at 650 °C, corresponding to their highest performance P_{max}. It is known that the resistance of the cell is greatly dependent on the operating temperature. This temperature dependence can be described using the Arrhenius empirical equation:

$$\ln(\sigma) = \ln(A) - \frac{E_a}{RT},$$

where σ is the conductivity of the single cell equivalent to the reciprocal of ASR, E_a is the activation energy in eV, R is the gas constant, T is the absolute temperature of operation, and A is a constant independent of temperature.

Table 4. The electrochemical properties (including Pmax, Open Circuit Voltage (OCV), Area-Specific Resistance (ASR), lnσ, and calculated activation energy E_a) of SOFC-reduced cells operated at various temperatures (500 to 650 °C) under air and a mixture of H_2/(3%) H_2O (n.d. = non defined due to OCV < 0.7 V).

	Operating Temperature (°C)	P_{max} (mW·cm^{-2})	OCV (mV)	ASR (Ω·cm^2)	lnσ (S·cm^{-1})	Activation Energy E_a (eV)
Sample 1	500	23.5	920	8.13	−8.60	0.70
	550	38.5	862	3.89	−7.86	
	600	47	785	2.44	−7.39	
	650	31.5	667	n.d.	n.d.	
Sample 2	500	150	880	1.26	−5.83	0.43
	550	190	820	0.80	−5.38	
	600	110	725	0.61	−5.10	
	650	110	618	n.d.	n.d.	
Sample 3	500	82	950	2.72	−7.17	0.63
	550	121	914	1.78	−6.74	
	600	176	880	1.08	−6.24	
	650	225	800	0.66	−5.75	
Sample 4	500	145	950	1.73	−6.76	0.58
	550	226	905	0.92	−6.13	
	600	307	875	0.60	−5.70	
	650	366	800	0.36	−5.19	

The conductivity values of the four studied samples are in the range of other published results [23–25]. The conductivities of the cells are thus plotted logarithmically versus 1000/T, as shown in Figure 5, to calculate E_a, and the results are listed in Table 4. It is apparent that sample 2 obtains the lowest E_a of 0.43 eV in comparison with the other cells. Sample 1 exhibits the highest value of activation energy of 0.70 eV and the lowest conductivity. Samples 3 and 4 have "intermediate" values of 0.63 and 0.58 eV, respectively.
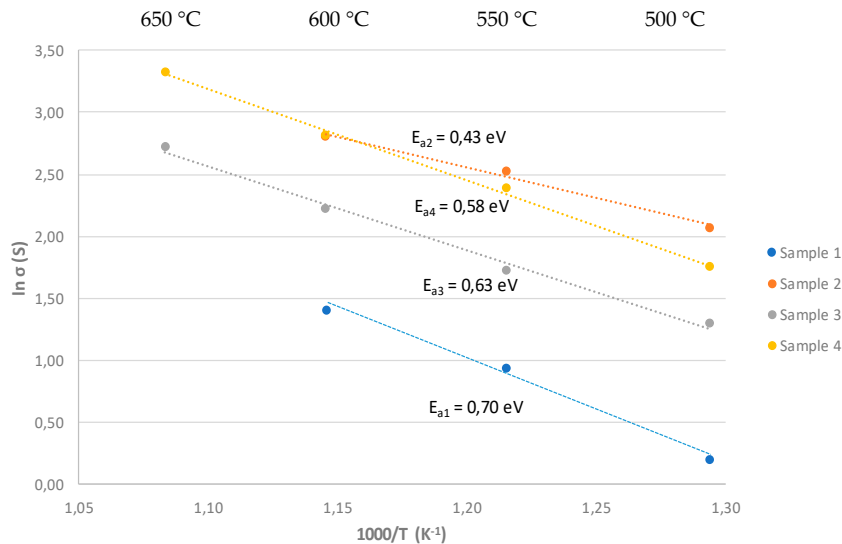
Figure 5. ln σ versus 1000/T for the 4 studied samples.

The anode support layer thicknesses with or without the Anode Functional Layer, varying from 260 to 278 µm, are practically the same for all the samples. Sample 1, exhibiting a low thickness of the cathode layer of 9 µm and electrolyte layer of 15 µm, gives the lowest performance: P_{max} = 47 mW·cm^{-2}. The oxygen reduction in the Mixed Ionic and Electronic Material (MIEC) material LSCF can be divided into several elemental steps [26–28]: (1) adsorption of O_2 onto the surface; (2) dissociation of the absorbed O_2 into oxygen atoms on the surface with charge transfer and oxygen incorporation at the MIEC interface; (3) surface diffusion of adsorbed oxygen on the MIEC surface; (4) bulk diffusion of adsorbed of O_2 in the bulk phase; (5) O_2 transfer at the interface between the MIEC and the electrolyte; (6) charge transfer and the incorporation of adsorbed oxygen at the TPB.

The oxygen reduction reaction rate can be influenced by any of these basic steps. As presented in a previous study [29], if the thickness of the cathode is too low, the efficiency of these previous elemental steps is not optimum. Consequently, sample 1 shows the lowest conductivity, the highest activation energy, and the worst power density performance. Sample 2 presents a thick electrolyte layer, with the power density of the cell reaching 150 mW·cm^{-2} at 500 °C. This high performance is in accordance with the lowest E_a value but cannot explain the low OCV value. Small cracks or pinholes were probably created during the fabrication process, and a direct contact between the H_2 and air was plausible. These cracks are not visible in the SEM. For this reason, the power density reaches a plateau, and the OCV values decrease dramatically with the increasing temperature. It is then impossible to give a conclusion on the electrolyte thickness effect. Finally, decreasing the thickness of the electrolyte to 20 µm while keeping the cathode thickness close to 50 µm, as in samples 3 and 4, allows to obtain the best results in terms of power density. Besides this, sample 4 exhibits a higher conductivity and also a lower activation energy than sample 3 leading to a better power density performance. The main AFL functions are to provide a flat surface for the electrolyte layer and to adjust the thermal expansion coefficient between the porous anode and the dense electrolyte. Even if the AFL, present in sample 3, plays its mechanical role, it slows down the chemical reactions, particularly the hydrogen diffusion at the TPB. However, sample 4 without an AFL layer exhibits the best performance in terms of power

density. This being said a priori, this is linked to the greater efficiency of the hydrogen oxidation reaction on the anodic side.

4. Conclusions

Anode-supported planar cells Ni-GDC//GDC//LSCF-GDC with a $10 \, \text{cm}^2$ active surface were shaped by a tape casting process before sintering at 1215 °C. The power density performances of four cells, differing by their cathode thickness and the presence of an AFL, were reported in the temperature range of 500 to 650 °C. The best performance, $368 \, \text{mW·cm}^{-2}$, was obtained for a cathode thickness of 50 μm and an electrolyte thickness of 20 μm. When the cathode thickness decreases, the power density decreases due to the limited oxygen integration. The ohmic potentials were calculated, and the results show that the electrolyte contribution is the preponderant factor in the potential decrease, while the activation and concentration overpotentials are almost negligible. The microstructure of the electrolyte leading to low values of conductivity seems to be the main reason. The activation energy has been concurrently determined, and the maximum value, 0.70 eV, corresponds to the sample with the lowest cathode/electrolyte thickness. The intermediate values of activation energies close to 0.60 eV are for samples 3 and 4, which respectively have a power density of 225 and $366 \, \text{mW·cm}^{-2}$. Assuming that the cathode and electrolyte layers have the same thicknesses for both samples, the power density difference is due to the presence of AFL in sample 3. This result, which shows a negative impact of the AFL on the power density performance, is surprising and is not in accordance with the common literature [30,31]. The absence of a TPB combined with the thickness and microstructure of the AFL could be a reason for the lower power density measured.

Author Contributions: Conceptualization, L.C. and G.C.; data curation, V.S. and M.F.; formal analysis, V.S., M.F., L.C. and G.C.; funding acquisition, L.C. and G.C.; investigation, V.S.; methodology, V.S., L.C., M.F. and G.C.; Project administration, L.C. and G.C.; resources, G.C. and L.C.; software, none; supervision, G.C.; visualization, V.S. and M.F.; writing—original draft preparation, V.S., M.F., L.C. and G.C.; writing—review and editing, G.C. and L.C. All authors have read and agreed to the published version of the manuscript.

Conflicts of Interest: The authors declare no conflict of interest.

References

1. Minh, N.Q. Ceramic Fuel Cells. *J. Am. Ceram. Soc.* **1993**, *76*, 563–588. [CrossRef]
2. Brett, D.J.L.; Atkinson, A.; Brandon, N.P.; Skinner, S.J. Intermediate temperature solid oxide fuel cells. *Chem. Soc. Rev.* **2008**, *37*, 1568–1578. [CrossRef]
3. Saeba, D.; Authayanum, S.; Patcharavorachot, Y.; Chatrattanawet, N.; Arpornwichanop, A. Electrochemical performance assessment of low-temperature solid oxide fuel cell with YSZ-based and SDC-based electrolytes. *Int. J. Hydrog. Energy* **2018**, *43*, 921–931. [CrossRef]
4. Steele, B.C.H.; Heinzel, A. Materials for fuel-cell technologies. *Nature* **2001**, *414*, 345–352. [CrossRef]
5. Kharton, V.V.; Figueiredo, F.M.; Navarro, L.; Naumovich, E.N.; Kovalevsky, A.V.; Yaremchenko, A.A.; Viskup, A.P.; Carneiro, A.; Marques, F.M.B.; Frade, J.R. Ceria-based materials for solid oxide fuel cells. *J. Mater. Sci.* **2001**, *36*, 1105–1117. [CrossRef]
6. Wandekar, R.V.; Basu, M.A.; Wani, B.N.; Bharadwaj, S.R. Physicochemical studies of NiO–GDC composites. *Mater. Chem. Phys.* **2006**, *99*, 289–294. [CrossRef]
7. Prokop, T.A.; Berent, K.; Iwai, H.; Szmyd, J.S.; Brus, G. A three-dimensional heterogeneity analysis of electrochemical energy conversion in SOFC anodes using electron nanotomography and mathematical modeling. *Int. J. Hydrog. Energy* **2018**, *43*, 10016–10030. [CrossRef]
8. Murray, E.P.; Barnett, S.A. (La,Sr)MnO$_3$–(Ce,Gd)O$_{2-x}$ composite cathodes for solid oxide fuel cells. *Solid State Ion.* **2001**, *143*, 265–273. [CrossRef]
9. Lee, S.J.; Muralidharan, P.; Jo, S.H.; Kim, D.K. Composite cathode for IT-SOFC: Sr-doped lanthanum cuprate and Gd-doped ceria. *Electrochem. Comm.* **2010**, *12*, 808–811. [CrossRef]

10. Leng, Y.J.; Chan, S.H.; Khor, K.A.; Jiang, S.P. $(La_{0.8}Sr_{0.2})_{0.9}MnO_3$-$Gd_{0.2}Ce_{0.8}O_{1.9}$ composite cathodes prepared from $(Gd,Ce)(NO_3)_x$ -modified $(La_{0.8}Sr_{0.2})_{0.9}MnO_3$ for intermediate-temperature solid oxide fuel cells. *J. Solid State Electrochem.* **2006**, *10*, 339–347. [CrossRef]

11. Wang, Z.; Zhang, N.; Qiao, J.; Sun, K.; Xu, P. Improved SOFC performance with continuously graded anode functional layer. *Electrochem. Commun.* **2009**, *11*, 1120–1123. [CrossRef]

12. Sivasankaran, V.; Combemale, L.; Pera, M.-C.; Caboche, G. Initial Preparation and Characterization of Single Step Fabricated Intermediate Temperature Solid Oxide Fuel Cells (IT-SOFC). *Fuel Cells* **2014**, *14*, 533–536. [CrossRef]

13. Sivasankaran, V. Manufacturing and Characterization of Single Cell Intermediate Temperature Solid Oxide Fuel Cells for APU in Transportation Application. Ph.D. Thesis, University of Burgundy, Dijon, France, July 2014.

14. Sivasankaran, V.; Combemale, L.; Caboche, G. Method of Preparing a Fuel Cell. WO2014057218A2, 9 September 2013. PCT/FR2013/052408 World Patent.

15. Raju, K.; Kim, S.; Hyung, C.J.; Yu, J.H.; Seong, Y.-H.; Kim, S.-H.; Han, I.-S. Optimal sintering temperature for $Ce_{0.9}Gd_{0.1}O_{2-\delta}$–$La_{0.6}Sr_{0.4}Co_{0.2}Fe_{0.8}O_{3-\delta}$ composites evaluated through their microstructural, mechanical and elastic properties. *Ceram. Int.* **2019**, *45*, 1460–1463. [CrossRef]

16. Li, J.; Lv, T.; Dong, X.; Yu, J.; Yu, B.; Li, P.; Yao, X.; Zhao, Y.; Li, Y. Linear discharge model, power losses and overall efficiency of solid oxide fuel cell with thin film Sm doped ceria electrolyte. Part II: Power losses overall efficiency. *Int. J. Hydrog. Energy* **2017**, *42*, 17522–17527. [CrossRef]

17. Chiodelli, G.; Malavasi, L. Electrochemical open circuit voltage (OCV) characterization of SOFC materials. *Ionics* **2013**, *19*, 1135–1144. [CrossRef]

18. Sindiraç, C.; Büyükaksoy, A.; Akkurt, S. Electrical properties of gadolinia doped ceria electrolytes fabricated by infiltration aided sintering. *Solid State Ion.* **2019**, *340*, 115020–115028. [CrossRef]

19. Lubini, M.; Chinarro, E.; Moreno, B.; De Sousa, V.C.; Alves, A.K.; Bergmann, C.P. Electrical properties of $La_{0.6}Sr_{0.4}Co_{1-y}Fe_yO_3$ (y = 0.2–1.0) fibers obtained by electrospinning. *J. Phys. Chem.* **2016**, *120*, 64–69. [CrossRef]

20. Bianchi, F.R.; Bosio, B.; Baldinelli, A.; Barelli, L. Optimisation of a reference kinetic model for Solid Oxide Fuel Cells. *Catalysts* **2020**, *10*, 104. [CrossRef]

21. Hauch, A.; Mogensen, M.B. Testing of Electrodes, Cells, and Short Stacks. In *Advances in Medium and High Temperature Solid Oxide Fuel Cell Technology*; CISM International Centre for Mechanical Sciences: Udine, Italy, 2009; Volume 574, pp. 31–76. [CrossRef]

22. Li, T.; Wang, W.G.; Miao, H.; Chen, T.; Xu, C. Effect of reduction temperature on the electrochemical properties of a Ni/YSZ anode-supported solid oxide fuel cell. *J. Alloys Compd.* **2010**, *495*, 138–143. [CrossRef]

23. Zhen, Y.D.; Tok, A.I.Y.; Jiang, S.P.; Boey, F.Y.C. Fabrication and performance of gadolinia-doped ceria-based intermediate-temperature solid oxide fuel cells. *J. Power Sourc.* **2008**, *178*, 69–74. [CrossRef]

24. Yamaguchi, T.; Shimizu, S.; Suzuki, T.; Fujishiro, Y.; Awano, M. Fabrication and characterization of high performance cathode supported small-scale SOFC for intermediate temperature operation. *Electrochem. Commun.* **2008**, *10*, 1381–1383. [CrossRef]

25. Ding, C.; Lin, H.; Sato, K.; Hashida, T. A simple rapid spray method for preparing anode-supported solid oxide fuel cells with GDC electrolyte thin films. *J. Membr. Sci.* **2010**, *350*, 1–4. [CrossRef]

26. Gao, Z.; Liu, X.M.; Bergman, B.; Zhao, Z. Investigation of oxygen reduction reaction kinetics on $Sm_{0.5}Sr_{0.5}CoO_{3-\delta}$ cathode supported on $Ce_{0.85}Sm_{0.075}Nd_{0.075}O_{2-\delta}$ electrolyte. *J. Power Sourc.* **2011**, *196*, 9195–9203. [CrossRef]

27. Han, D.; Wu, H.; Li, J.L.; Wang, S.R.; Zhan, Z.L. Nanostructuring of $SmBa_{0.5}Sr_{0.5}Co_2O_{5+\delta}$ cathodes for reduced-temperature solid oxide fuel cells. *J. Power Sourc.* **2014**, *246*, 409–416. [CrossRef]

28. Horita, T.; Yamaji, K.; Sakai, N.; Yokokawa, H.; Weber, A.; Ivers-Tiffée, E. Oxygen reduction mechanism at porous $La_{1-x}Sr_xCoO_{3-d}$ cathodes/$La_{0.8}Sr_{0.2}Ga_{0.8}Mg_{0.2}O_{2.8}$ electrolyte interface for solid oxide fuel cells. *Electrochim. Acta* **2001**, *46*, 1837–1845. [CrossRef]

29. Li, W.; Shi, Y.; Luo, Y.; Cai, N. Theoretical modeling of air electrode operating in SOFC mode and SOEC mode: The effects of microstructure and thickness. *Int. J. Hydrog. Energy* **2014**, *39*, 13738–13750. [CrossRef]

30. Bi, L.; Fabbri, E.; Traversa, E. Effect of anode functional layer on the performance of proton-conducting solid oxide fuel cells (SOFCs). *Electrochem. Commun.* **2012**, *16*, 37–40. [CrossRef]

31. Suzuki, T.; Sugihara, S.; Yamaguchi, T.; Sumi, H.; Hamamoto, K.; Fujishiro, Y. Effect of anode functional layer on energy efficiency of solid oxide fuel cells. *Electrochem. Commun.* **2011**, *13*, 959–962. [CrossRef]